SESAM modelocked Yb:$CaGdAlO_4$ laser in the soliton modelocking regime with positive intracavity dispersion

C. R. Phillips,* A. S. Mayer, A. Klenner, and U. Keller

Department of Physics, Institute of Quantum Electronics, ETH Zurich, 8093 Zurich, Switzerland

*cphillips@phys.ethz.ch

Abstract: We demonstrate femtosecond SESAM modelocking in the near-infrared by using cascaded quadratic nonlinearities (phase-mismatched second-harmonic generation, SHG), enabling soliton modelocking in the normal dispersion regime without any dispersion compensating elements. To obtain large and negative self-phase modulation (SPM) we use an intracavity LBO crystal, whose temperature and angles are optimized with respect to SPM, nonlinear losses, and self-starting characteristics. To support femtosecond pulses, we use the very promising Yb:$CaGdAlO_4$ (CALGO) gain material, operated in a bulk configuration. The LBO crystal provides sufficient negative SPM to compensate for its own GDD as well as the positive GDD and SPM from the gain crystal. The modelocked laser produces pulses of 114 fs at 1050 nm, with a repetition rate of 113 MHz (average output power 1.1 W). We perform a detailed theoretical study of this soliton modelocking regime with positive GDD, which clearly indicates the important design constraints in an intuitive and systematic way. In particular, due to its importance in avoiding multi-pulsed modelocking, we examine the nonlinear loss associated with the cascading process carefully and show how it can be suppressed in practice. With this modelocking regime, it should be possible to overcome the limits faced by current state of the art modelocked lasers in terms of dispersion compensation and nonlinearity management at high powers, suppression of Q-switching in compact GHz lasers, and enabling femtosecond soliton modelocking at very high repetition rates due to the high nonlinearities accessible via cascading combined with eliminating the need for intracavity dispersion compensation.

OCIS codes: (140.7090) Ultrafast lasers; (140.4050) Mode-locked lasers; (190.5530) Pulse propagation and temporal solitons.

References and links

1. L. F. Mollenauer and R. H. Stolen, "The soliton laser," Opt. Lett. **9**, 13–15 (1984).
2. U. Keller, K. Weingarten, F. X. Kärtner, D. Kopf, B. Braun, I. Jung, R. Fluck, C. Hönninger, N. Matuschek, and J. Aus der Au, "Semiconductor saturable absorber mirrors (SESAM's) for femtosecond to nanosecond pulse generation in solid-state lasers," Selected Topics in Quantum Electronics, IEEE Journal of **2**, 435–453 (1996).
3. F. X. Kärtner and U. Keller, "Stabilization of solitonlike pulses with a slow saturable absorber," Opt. Lett. **20**, 16–18 (1995).

#205464 - $15.00 USD Received 27 Jan 2014; accepted 25 Feb 2014; published 6 Mar 2014

4. F. X. Kärtner, I. Jung, and U. Keller, "Soliton mode-locking with saturable absorbers," Selected Topics in Quantum Electronics, IEEE Journal of **2**, 540–556 (1996).
5. U. Keller, "Ultrafast solid-state laser oscillators: a success story for the last 20 years with no end in sight," Applied Physics B **100**, 15–28 (2010).
6. F. X. Kärtner, D. Kopf, and U. Keller, "Solitary-pulse stabilization and shortening in actively mode-locked lasers," J. Opt. Soc. Am. B **12**, 486–496 (1995).
7. I. D. Jung, F. X. Kärtner, L. R. Brovelli, M. Kamp, and U. Keller, "Experimental verification of soliton mode locking using only a slow saturable absorber," Opt. Lett. **20**, 1892–1894 (1995).
8. C. Saraceno, C. Schriber, M. Mangold, M. Hoffmann, O. Heckl, C. Baer, M. Golling, T. Südmeyer, and U. Keller, "SESAMs for high-power oscillators: Design guidelines and damage thresholds," Selected Topics in Quantum Electronics, IEEE Journal of **18**, 29–41 (2012).
9. R. Paschotta, R. Hring, A. Garnache, S. Hoogland, A. Tropper, and U. Keller, "Soliton-like pulse-shaping mechanism in passively mode-locked surface-emitting semiconductor lasers," Applied Physics B **75**, 445–451 (2002).
10. M. Hoffmann, O. D. Sieber, D. J. H. C. Maas, V. J. Wittwer, M. Golling, T. Südmeyer, and U. Keller, "Experimental verification of soliton-like pulse-shaping mechanisms in passively mode-locked VECSELs," Opt. Express **18**, 10143–10153 (2010).
11. R. Schiek, "Nonlinear refraction caused by cascaded second-order nonlinearity in optical waveguide structures," J. Opt. Soc. Am. B **10**, 1848–1855 (1993).
12. G. I. Stegeman, D. J. Hagan, and L. Torner, "$\chi^{(2)}$ cascading phenomena and their applications to all-optical signal processing, mode-locking, pulse compression and solitons," Optical and Quantum Electronics **28**, 1691–1740 (1996).
13. D. Bauer, I. Zawischa, D. H. Sutter, A. Killi, and T. Dekorsy, "Mode-locked Yb:YAG thin-disk oscillator with 41 µJ pulse energy at 145 W average infrared power and high power frequency conversion," Opt. Express **20**, 9698–9704 (2012).
14. C. J. Saraceno, F. Emaury, O. H. Heckl, C. R. E. Baer, M. Hoffmann, C. Schriber, M. Golling, T. Südmeyer, and U. Keller, "275 W average output power from a femtosecond thin disk oscillator operated in a vacuum environment," Opt. Express **20**, 23535–23541 (2012).
15. C. J. Saraceno, F. Emaury, C. Schriber, M. Hoffmann, M. Golling, T. Südmeyer, and U. Keller, "Ultrafast thin-disk laser with 80 μJ pulse energy and 242 W of average power," Opt. Lett. **39**, 9–12 (2014).
16. T. R. Schibli, I. Hartl, D. C. Yost, M. J. Martin, A. Marcinkevičius, M. E. Fermann, and J. Ye, "Optical frequency comb with submillihertz linewidth and more than 10 W average power," Nature Photonics **2**, 355–359 (2008).
17. S. Witte and K. Eikema, "Ultrafast optical parametric Chirped-Pulse amplification," Selected Topics in IEEE J. Quant. Electron. **18**, 296–307 (2012).
18. F. Krausz and M. Ivanov, "Attosecond physics," Rev. Mod. Phys. **81**, 163–234 (2009).
19. D. Hillerkuss, R. Schmogrow, T. Schellinger, M. Jordan, M. Winter, G. Huber, T. Vallaitis, R. Bonk, P. Kleinow, F. Frey, M. Roeger, S. Koenig, A. Ludwig, A. Marculescu, J. Li, M. Hoh, M. Dreschmann, J. Meyer, S. Ben Ezra, N. Narkiss, B. Nebendahl, F. Parmigiani, P. Petropoulos, B. Resan, A. Oehler, K. Weingarten, T. Ellermeyer, J. Lutz, M. Moeller, M. Huebner, J. Becker, C. Koos, W. Freude, and J. Leuthold, "26 Tbit s^{-1} line-rate super-channel transmission utilizing all-optical fast fourier transform processing," Nature Photonics **5**, 364–371 (2011).
20. S. A. Diddams, "The evolving optical frequency comb [Invited]," J. Opt. Soc. Am. B **27**, B51–B62 (2010).
21. T. M. Fortier, A. Bartels, and S. A. Diddams, "Octave-spanning Ti:sapphire laser with a repetition rate $>$1 GHz for optical frequency measurements and comparisons," Opt. Lett. **31**, 1011–1013 (2006).
22. J. M. Dudley, G. Genty, and S. Coen, "Supercontinuum generation in photonic crystal fiber," Reviews of Modern Physics **78**, 1135 (2006).
23. A. Klenner, M. Golling, and U. Keller, "A gigahertz multimode-diode-pumped Yb:KGW enables a strong frequency comb offset beat signal," Opt. Express **21**, 10351–10357 (2013).
24. U. Keller and A. C. Tropper, "Passively modelocked surface-emitting semiconductor lasers," Physics Reports **429**, 67–120 (2006).
25. D. J. H. C. Maas, A.-R. Bellancourt, B. Rudin, M. Golling, H. J. Unold, T. Südmeyer, and U. Keller, "Vertical integration of ultrafast semiconductor lasers," Applied Physics B **88**, 493–497 (2007).
26. M. Mangold, C. A. Zaugg, S. M. Link, M. Golling, B. W. Tilma, and U. Keller, "Pulse repetition rate tuning from 5 to 100 GHz with a high-power semiconductor disk laser," Opt. Express (to be published).
27. A. Klenner, F. Emaury, C. Schriber, A. Diebold, C. J. Saraceno, S. Schilt, U. Keller, and T. Südmeyer, "Phase-stabilization of the carrier-envelope-offset frequency of a SESAM modelocked thin disk laser," Opt. Express **21**, 24770–24780 (2013).
28. U. Keller, "Ultrafast solid-state lasers," in *Landolt-Börnstein, Laser Physics and Applications, Subvolume B: Laser Systems, Part I.*, G. Herziger, H. Weber, and R. Poprawe, eds. (Springer-Verlag, Heidelberg, 2007), pp. 33–167.
29. V. Pervak, O. Pronin, O. Razskazovskaya, J. Brons, I. B. Angelov, M. K. Trubetskov, A. V. Tikhonravov, and F. Krausz, "High-dispersive mirrors for high power applications," Opt. Express **20**, 4503–4508 (2012).
30. R. Szipöcs, C. Spielmann, F. Krausz, and K. Ferencz, "Chirped multilayer coatings for broadband dispersion control in femtosecond lasers," Opt. Lett. **19**, 201–203 (1994).

#205464 - $15.00 USD Received 27 Jan 2014; accepted 25 Feb 2014; published 6 Mar 2014

31. N. Matuschek, F. X. Kärtner, and U. Keller, "Theory of double-chirped mirrors," Selected Topics in Quantum Electronics, IEEE Journal of **4**, 197–208 (1998).
32. R. DeSalvo, A. Said, D. Hagan, E. Van Stryland, and M. Sheik-Bahae, "Infrared to ultraviolet measurements of two-photon absorption and n_2 in wide bandgap solids," IEEE J. Quant. Electron. **32**, 1324–1333 (1996).
33. S. V. Marchese, C. R. Baer, A. G. Engqvist, S. Hashimoto, D. J. H. C. Maas, M. Golling, T. Südmeyer, and U. Keller, "Femtosecond thin disk laser oscillator with pulse energy beyond the 10-microjoule level," Opt. Express **16**, 6397–6407 (2008).
34. F. O. Ilday and F. W. Wise, "Nonlinearity management: a route to high-energy soliton fiber lasers," J. Opt. Soc. Am. B **19**, 470–476 (2002).
35. X. Liu, L. Qian, and F. Wise, "High-energy pulse compression by use of negative phase shifts produced by the cascade $\chi^{(2)} : \chi^{(2)}$ nonlinearity," Opt. Lett. **24**, 1777–1779 (1999).
36. S. Ashihara, J. Nishina, T. Shimura, and K. Kuroda, "Soliton compression of femtosecond pulses in quadratic media," J. Opt. Soc. Am. B **19**, 2505–2510 (2002).
37. J. Moses and F. W. Wise, "Soliton compression in quadratic media: high-energy few-cycle pulses with a frequency-doubling crystal," Opt. Lett. **31**, 1881–1883 (2006).
38. F. O. Ilday, K. Beckwitt, Y.-F. Chen, H. Lim, and F. W. Wise, "Controllable raman-like nonlinearities from nonstationary, cascaded quadratic processes," J. Opt. Soc. Am. B **21**, 376–383 (2004).
39. C. Langrock, M. M. Fejer, I. Hartl, and M. E. Fermann, "Generation of octave-spanning spectra inside reverse-proton-exchanged periodically poled lithium niobate waveguides," Opt. Lett. **32**, 2478–2480 (2007).
40. C. R. Phillips, C. Langrock, J. S. Pelc, M. M. Fejer, I. Hartl, and M. E. Fermann, "Supercontinuum generation in quasi-phasematched waveguides," Opt. Express **19**, 18754–18773 (2011).
41. C. R. Phillips, C. Langrock, J. S. Pelc, M. M. Fejer, J. Jiang, M. E. Fermann, and I. Hartl, "Supercontinuum generation in quasi-phase-matched $LiNbO_3$ waveguide pumped by a Tm-doped fiber laser system," Opt. Lett. **36**, 3912–3914 (2011).
42. V. Ulvila, C. R. Phillips, L. Halonen, and M. Vainio, "Frequency comb generation by a continuous-wave-pumped optical parametric oscillator based on cascading quadratic nonlinearities," Opt. Lett. **38**, 4281–4284 (2013).
43. C. R. Phillips and M. M. Fejer, "Efficiency and phase of optical parametric amplification in chirped quasi-phase-matched gratings," Opt. Lett. **35**, 3093–3095 (2010).
44. C. R. Phillips and M. M. Fejer, "Adiabatic optical parametric oscillators: steady-state and dynamical behavior," Opt. Express **20**, 2466–2482 (2012).
45. C. R. Phillips, C. Langrock, D. Chang, Y. W. Lin, L. Gallmann, and M. M. Fejer, "Apodization of chirped quasi-phasematching devices," J. Opt. Soc. Am. B **30**, 1551–1568 (2013).
46. L. Qian, X. Liu, and F. Wise, "Femtosecond kerr-lens mode locking with negative nonlinear phase shifts," Opt. Lett. **24**, 166–168 (1999).
47. M. Zavelani-Rossi, G. Cerullo, and V. Magni, "Mode locking by cascading of second-order nonlinearities," Quantum Electronics, IEEE Journal of **34**, 61–70 (1998).
48. A. Agnesi, A. Guandalini, and G. Reali, "Self-stabilized and dispersion-compensated passively mode-locked Yb:Yttrium aluminum garnet laser," Applied Physics Letters **86**, 171105 (2005).
49. A. Agnesi, L. Carrà, F. Pirzio, and G. Reali, "Femtosecond Nd:glass oscillator operating in normal dispersion regime," Opt. Express **16**, 9549–9553 (2008).
50. R. W. Boyd, *Nonlinear Optics* (Academic, 2008, 3rd edition).
51. K. Kato, "Temperature-tuned 90° phase-matching properties of LiB_3O_5," Quantum Electronics, IEEE Journal of **30**, 2950–2952 (1994).
52. D. A. Roberts, "Simplified characterization of uniaxial and biaxial nonlinear optical-crystals: a plea for standardization of nomenclature and conventions," IEEE J. Quantum. Electron. **28**, 2057–2074 (1992).
53. M. Sheik-Bahae and M. Ebrahimzadeh, "Measurements of nonlinear refraction in the second-order $\chi^{(2)}$ materials $KTiOPO_4$, $KNbO_3$, β-BaB_2O_4, and LiB_3O_5," Optics Communications **142**, 294–298 (1997).
54. B. Braun, F. Heine, T. Kellner, C. Hönninger, G. Zhang, G. Huber, and U. Keller, "Efficient intracavity frequency doubling of a passively mode-locked diode-pumped neodymium lanthanum scandium borate laser," Opt. Lett. **21**, 1567–1569 (1996).
55. G. Imeshev, M. A. Arbore, S. Kasriel, and M. M. Fejer, "Pulse shaping and compression by second-harmonic generation with quasi-phase-matching gratings in the presence of arbitrary dispersion," J. Opt. Soc. Am. B **17**, 1420–1437 (2000).
56. G. P. Agrawal, *Nonlinear Fiber Optics* (Academic, 2006).
57. C. R. Phillips, L. Gallmann, and M. M. Fejer, "Design of quasi-phasematching gratings via convex optimization," Opt. Express **21**, 10139–10159 (2013).
58. C. Conti, S. Trillo, P. Di Trapani, J. Kilius, A. Bramati, S. Minardi, W. Chinaglia, and G. Valiulis, "Effective lensing effects in parametric frequency conversion," J. Opt. Soc. Am. B **19**, 852 (2002).
59. G. G. Luther, M. S. Alber, J. E. Marsden, and J. M. Robbins, "Geometric analysis of optical frequency conversion and its control in quadratic nonlinear media," J. Opt. Soc. Am. B **17**, 932–941 (2000).
60. C. Hönninger, R. Paschotta, F. Morier-Genoud, M. Moser, and U. Keller, "Q-switching stability limits of continuous-wave passive mode locking," J. Opt. Soc. Am. B **16**, 46–56 (1999).

#205464 - $15.00 USD Received 27 Jan 2014; accepted 25 Feb 2014; published 6 Mar 2014

61. R. Grange, M. Haiml, R. Paschotta, G. Spühler, L. Krainer, M. Golling, O. Ostinelli, and U. Keller, "New regime of inverse saturable absorption for self-stabilizing passively mode-locked lasers," Applied Physics B **80**, 151–158 (2005).
62. H. A. Haus and E. P. Ippen, "Self-starting of passively mode-locked lasers," Opt. Lett. **16**, 1331–1333 (1991).
63. J. Petit, P. Goldner, and B. Viana, "Laser emission with low quantum defect in Yb:$CaGdAlO_4$," Opt. Lett. **30**, 1345–1347 (2005).
64. A. Diebold, F. Emaury, C. Schriber, M. Golling, C. J. Saraceno, T. Südmeyer, and U. Keller, "SESAM mode-locked Yb:$CaGdAlO_4$ thin disk laser with 62 fs pulse generation," Opt. Lett. **38**, 3842–3845 (2013).
65. Y. Zaouter, J. Didierjean, F. Balembois, G. L. Leclin, F. Druon, P. Georges, J. Petit, P. Goldner, and B. Viana, "47-fs diode-pumped Yb^{3+}:$CaGdAlO_4$ laser," Opt. Lett. **31**, 119–121 (2006).
66. A. Agnesi, A. Greborio, F. Pirzio, G. Reali, J. A. der Au, and A. Guandalini, "40-fs Yb^{3+}:$CaGdAlO_4$ laser pumped by a single-mode 350-mW laser diode," Opt. Express **20**, 10077–10082 (2012).
67. A. Greborio, A. Guandalini, and J. Aus der Au, "Sub-100 fs pulses with 12.5-W from Yb:CALGO based oscillators," in "Society of Photo-Optical Instrumentation Engineers (SPIE) Conference Series," , vol. 8235 of *Society of Photo-Optical Instrumentation Engineers (SPIE) Conference Series* (2012), vol. 8235 of *Society of Photo-Optical Instrumentation Engineers (SPIE) Conference Series*.
68. S. Ricaud, A. Jaffres, K. Wentsch, A. Suganuma, B. Viana, P. Loiseau, B. Weichelt, M. Abdou-Ahmed, A. Voss, T. Graf, D. Rytz, C. Hönninger, E. Mottay, P. Georges, and F. Druon, "Femtosecond Yb:$CaGdAlO_4$ thin-disk oscillator," Opt. Lett. **37**, 3984–3986 (2012).
69. K. Beil, B. Deppe, and C. Kränkel, "Yb:$CaGdAlO_4$ thin-disk laser with 70% slope efficiency and 90 nm wavelength tuning range," Opt. Lett. **38**, 1966–1968 (2013).
70. R. Paschotta, H. Telle, and U. Keller, "Noise of Solid-State Lasers," chapter 12 in *Solid-State Lasers and Applications*, Alphan Sennaroglu, editor. (CRC, Taylor and Francis Group, LLC, 2007).

1. Introduction

Since its introduction thirty years ago [1], soliton pulse formation for passive modelocking has formed the basis for an enormous variety of laser systems. When combined with semiconductor saturable absorber mirrors (SESAMs) [2–4], such lasers offer unparalleled performance in terms of average power and pulse energy, in combination with excellent reliability and stability [5].

In soliton modelocking, the pulse shaping is done solely by soliton formation, i.e. the balance of group delay dispersion (GDD) and self-phase modulation (SPM) at steady state [3, 4]. An additional loss mechanism, such as a saturable absorber [3, 4], or an acousto-optic modulator [6], is necessary to start the modelocking process and to stabilize the soliton pulse forming process. In soliton modelocking, we have shown that the net-gain window at steady state can remain open for significantly more than 10 times longer than the ultrashort pulse, depending on the specific laser parameters [4, 7]. This strongly relaxed the requirements on the SESAM and we can obtain ultrashort pulses even in the 10 fs regime with semiconductor saturable absorbers that have much longer recovery times. In addition, it also explained why stable modelocking was achieved with much more SPM than assumed to be allowed before [6]. The soliton modelocking was one of the main reasons why SESAM modelocking has become so successful, since nearly "any SESAM" worked out well as long as it was designed correctly to prevent damage [8].

So far, this soliton modelocking has been mostly applied in the negative GDD regime compensating the positive nonlinear refractive index change due to the Kerr effect typically obtained in the laser material. An exception was soliton modelocking with SESAM modelocked vertical external cavity surface emitting lasers (VECSELs) where an effective and non-instantaneous "negative SPM effect" was obtained with the combination of dynamic absorber and gain saturation [9, 10]. Here we demonstrate another regime of soliton modelocking where we introduce another effective "negative SPM effect", with a much faster nonlinear response, with cascaded quadratic nonlinearities using phase-mismatched second harmonic generation (SHG) [11, 12].

Our work is motivated by the continued advancement of modelocked laser technologies, especially in the low- and high-repetition rate regimes. For example, at low repetition rates of a

#205464 - $15.00 USD Received 27 Jan 2014; accepted 25 Feb 2014; published 6 Mar 2014

few megahertz, high-power thin disk lasers (TDLs) can offer very high energies and short pulses suited to applications such as machining and attosecond science [13–15]. Oscillator powers $>$270 W and energies 80 μJ have been demonstrated so far [14, 15]; such power-scalable lasers are making it possible to bridge the gap in energy between laser oscillators and amplifiers, opening up new possibilities for demanding applications such as high-power frequency combs [16], optical parametric chirped pulse amplification [17], and strong-field physics [18].

At high repetition rates, GHz frequency combs are pursued for applications in spectroscopy (where they offer unprecedented resolution for trace-gas detection), optical communications (offering ultra-high data rates [19]), and many other applications including metrology and low-noise microwave signal generation [20]. In Kerr lens modelocked (KLM) systems, octave-spanning GHz frequency combs have been demonstrated [21]. In the context of high-power SESAM-modelocked GHz combs, self-referencing has been demonstrated via supercontinuum generation [22] directly from bulk lasers [23], while modelocking of VECSELs [24] and modelocked integrated external-cavity surface emitting lasers (MIXSELs) [25] offer the potential for short pulses and scaling to high powers as well as extremely high repetition rates [26]. Combined with recent work in stabilizing thin disk lasers [27], and new broadband near-infrared (NIR) gain materials with excellent thermal properties such as Yb:$CaGdAlO_4$ (Yb:CALGO), these developments promise reliable, compact and high-power frequency combs generated with multi-mode-diode pumping.

The aforementioned lasers currently face a number of challenges relating to constraints on dispersion and nonlinearity. As such, alternative modelocking regimes offering greater flexibility may be required. In this paper, we demonstrate experimentally and analyze theoretically the use of cascaded quadratic nonlinearities in combination with SESAM modelocking, generating femtosecond pulses in the soliton modelocking regime, to offer additional options on how to resolve many of these challenges.

2. Motivation based on nonlinearity and dispersion

With respect to dispersion, bulk materials only exhibit negative group delay dispersion (GDD) coefficients at longer wavelengths within their transparency window: for lasers operating near or below 1 μm, bulk material dispersion is usually positive. Consequently, dispersion compensating mirrors (DMs), often in the form of Gires-Tournois interferometer-type mirrors (GTIs) are employed [28], and their performance continues to be advanced [29]. However, GTIs can limit performance in several ways, including their inherent trade-off between dispersion and bandwidth, as well as their increased susceptibility to damage and higher orders of dispersion due to the resonant structure. For GHz lasers, the small number of mirror bounces available can imply that individual mirrors must provide input/output coupling functionalities as well as a large and precise amount of dispersion compensation, which further constrains their design.

Chirped mirrors can exhibit broad bandwidths and do not involve a resonant structure [30, 31], but the dispersion they support is typically small compared with GTIs because of the limited group delay which can be introduced within the thin coating structure. Although prisms and gratings can be employed instead of DMs, this comes at the cost of increased alignment sensitivity and laser complexity.

In addition to the above constraints on DMs, the achievable nonlinear refractive indices (which we denote as n_2^{NL}) in transparent bulk media for NIR wavelengths is quite low and is positive, owing in part to the basic scaling of the third-order nonlinear susceptibility with the band-gap [32], in combination with the need to avoid two-photon absorption (TPA) in any bulk media placed inside the laser cavity. A low nonlinearity means that high intensities are needed, and is thus very relevant for high-repetition-rate lasers where much lower intensities are available. The opposite problem is encountered in low-repetition-rate / high-energy TDLs,

#205464 - $15.00 USD Received 27 Jan 2014; accepted 25 Feb 2014; published 6 Mar 2014

where the nonlinearity of the air inside the cavity is enough to destabilize the intracavity solitons [33]. To evade this issue, low-pressure chambers or complicated multi-pass arrangements are currently employed [13, 14, 33], adding to system cost and complexity.

An alternative modelocking regime, which has received comparatively very little attention, is to use a negative SPM and positive GDD. Cascaded quadratic nonlinearities support this regime by offering, simultaneously, large nonlinearities, negative effective nonlinear refractive indices, and positive GDD from material dispersion [11, 12]. These nonlinearities arise from phase-mismatched SHG, and can be characterized by the second-order nonlinear coefficient, denoted d_{eff}, as well as the phase mismatch $\Delta k_0 = k_2 - 2k_1$, where $k_j = n_j(\omega_j)\omega_j/c$ is the carrier wavevector of wave j. The characteristic property of cascading interaction is a large phase-mismatch Δk, in which a $\chi^{(3)}$-like SPM can be obtained instead of efficient SHG. For large $|\Delta k|$, the effective $\chi^{(3)}$ susceptibility associated with this cascading process yields a contribution to n_2^{NL} given by [12]

$$n_2^{\text{casc}} = -\frac{1}{\Delta k_0}\frac{4\pi d_{\text{eff}}^2}{n_1^2 n_2 \lambda_1 \varepsilon_0 c}, \tag{1}$$

where subscript 1 denotes the first-harmonic (FH) and subscript 2 denotes the second-harmonic (SH). An exception to this notation is the nonlinear refractive index: we use the superscripts on n_2^{NL} and n_2^{casc} to avoid confusion with the linear refractive index n_j of wave $j = 2$, the SH.

Based on Eq. (1), by adjusting Δk_0 via the orientation and temperature of SHG crystals, large, easily variable, and negative values of n_2^{NL} can be obtained. As such, this technique offers the potential for soliton formation without dispersion compensating mirrors and at potentially much lower intracavity intensities. Additionally, negative intracavity SPM could enable the compensation of large unwanted positive SPM contributions observed in high-energy lasers due to the nonlinearity of air. Compensating this SPM could mitigate or eliminate the need for the low-pressure or low-Q cavity configurations mentioned above [13, 14, 33]. SPM compensation via cascading has also been proposed in the context of fiber lasers [34].

Cascaded $\chi^{(2)}$ effects have been exploited for various applications [12], including pulse compression and frequency shifting [35–38], supercontinuum generation [39–41], and even in optical parametric oscillators [42]. The corresponding physics can also play an important role in efficient chirped phase-matching interactions, for example in parametric amplification involving chirped QPM devices [43–45].

Cascading has also been exploited for KLM [46, 47], in which the self-focusing/self-defocusing aspect of the nonlinear phase shifts was used to favor pulsed operation. SESAM modelocking with negative SPM using an LBO crystal was demonstrated in earlier work [48, 49], but there the design guidelines for the nonlinear crystal did not properly take into account the structure of the cascading interactions, which in turn limited the pulse durations which could be achieved to $>$0.5 ps [49].

To experimentally realize the potential of cascading in SESAM-modelocked lasers, and in particular to reach the femtosecond soliton modelocking regime, a detailed understanding of the nonlinear response is required, including the losses due to the small (but non-zero) SHG efficiency, and the corresponding perturbations on the soliton dynamics. In the rest of this paper, we first expand the theory of cascaded $\chi^{(2)}$ interactions in the context of modelocking (section 3). We then use that theory to develop laser design constraints for single-pulse self-starting SESAM modelocking (section 4). In section 5 we present an experimental demonstration of the technique, showing a SESAM-soliton-modelocked proof-of-principle laser using Yb:CALGO as the gain medium and LBO as the SHG crystal, which produces pulses of 114 fs at 1050 nm, with a repetition rate of 113 MHz (average power 1.1 W), operating without any dispersion compensating elements. We conclude and discuss the results in section 6.

#205464 - $15.00 USD Received 27 Jan 2014; accepted 25 Feb 2014; published 6 Mar 2014

3. Theory

In this section, we introduce the relevant theory and constraints for soliton modelocking via cascaded $\chi^{(2)}$. In subsection 3.1, we introduce the relevant coupled-wave equations for SHG, and simulate a typical cascading interaction. In subsections 3.2 and 3.3, we perform perturbative analyses to show and quantify the process, including nonlinear losses and non-instantaneous nonlinear responses.

3.1. Coupled wave equations

We use standard coupled-wave equations for SHG, assuming co-propagating waves, neglecting self-steepening effects for simplicity, but allowing for both dispersion and diffraction effects. The resulting equations are given by [50]

$$\left(\partial_z + \hat{D}_1\right) A_1 = -i\kappa_1 A_2 A_1^* e^{-i\Delta k_0 z} \tag{2a}$$

$$\left(\partial_z + \hat{D}_2\right) A_2 = -i\kappa_2 A_1^2 e^{i\Delta k_0 z}, \tag{2b}$$

where we have neglected $\chi^{(3)}$ effects for compactness. In these equations, $\partial_z = \partial/\partial z$, the coupling coefficients are defined as $\kappa_j = \omega_1 d_{\text{eff}}/(n_j c)$, and $\hat{D}_j$ are the operators describing diffraction, dispersion, and other linear-optical effects of the co-propagating electric field envelopes A_1 and A_2. For the relevant case where group velocity mismatch (GVM), group delay dispersion (GDD), and Poynting vector walkoff (PVW) effects are dominant, $\hat{D}_j$ are given by

$$\hat{D}_j = \rho_j \frac{\partial}{\partial x} + \delta_j \frac{\partial}{\partial t} - i\frac{\beta_j}{2}\frac{\partial^2}{\partial t^2}, \tag{3}$$

where ρ_j is the PVW coefficient (for transverse coordinate x), $\delta_j = (v_j^{-1} - v_{\text{ref}}^{-1})$ for group velocities v_j and arbitrary reference velocity v_{ref}, and $\beta_j = (\partial^2 k_j/\partial\omega^2)|_{\omega=\omega_j}$ is the GDD coefficient for wave j. These operators give rise to a frequency dependence of the phase mismatch. For the case of collinear plane waves, this phase mismatch is given by

$$\Delta k(\Omega_a, \Omega_b) = k_2(\omega_2 + \Omega_a + \Omega_b) - k_1(\omega_1 + \Omega_a) - k_1(\omega_1 + \Omega_b) \tag{4a}$$

$$\approx \Delta k_0 + (\delta_2 - \delta_1)(\Omega_a + \Omega_b), \tag{4b}$$

where $\Delta k_0 \equiv k_2(\omega_2) - 2k_1(\omega_1)$ is the phase mismatch evaluated at the carrier frequencies ω_1 and ω_2 of the FH and SH pulses, respectively. Equation (4b) applies for GVM-dominated interactions when GDD and higher orders of dispersion can be neglected when calculating Δk. A phase mismatch which only depends on the driven SH frequency is obtained in general when neglecting GDD and higher order terms of the FH. Note that we use upper case frequency variables (such as Ω_a and Ω_b above) to denote frequency shifts with respect to optical carrier frequencies ω_j.

The main features of the generated SH in a typical cascading interaction described by Eqs. (2) are depicted in Fig. 1, which shows the simulated evolution of the SH intensity versus delay and propagation distance, assuming parameters comparable to those obtained in our experimental system, described in section 5. Throughout the paper, we assume standard values for the dispersion and nonlinear coefficients of LBO [51–53]. The figure shows two pulse components of the SH: one propagating with the FH, the "main" pulse, and one propagating linearly, the "secondary" pulse. The main pulse causes $\chi^{(3)}$-like SPM of the FH according to Eq. (1), with a nonlinear phase shift proportional to $I_1/\Delta k_0$ for FH intensity I_1. Both SH pulse components have energy $\propto 1/\Delta k_0^2$, which corresponds to an intensity-dependent loss for the FH. Nonlinear losses from intracavity SHG can destabilize modelocking [54]. In the following subsections, we find approximate relations describing the response of the FH and SH envelopes in cascading regimes relevant for modelocking.

#205464 - $15.00 USD Received 27 Jan 2014; accepted 25 Feb 2014; published 6 Mar 2014

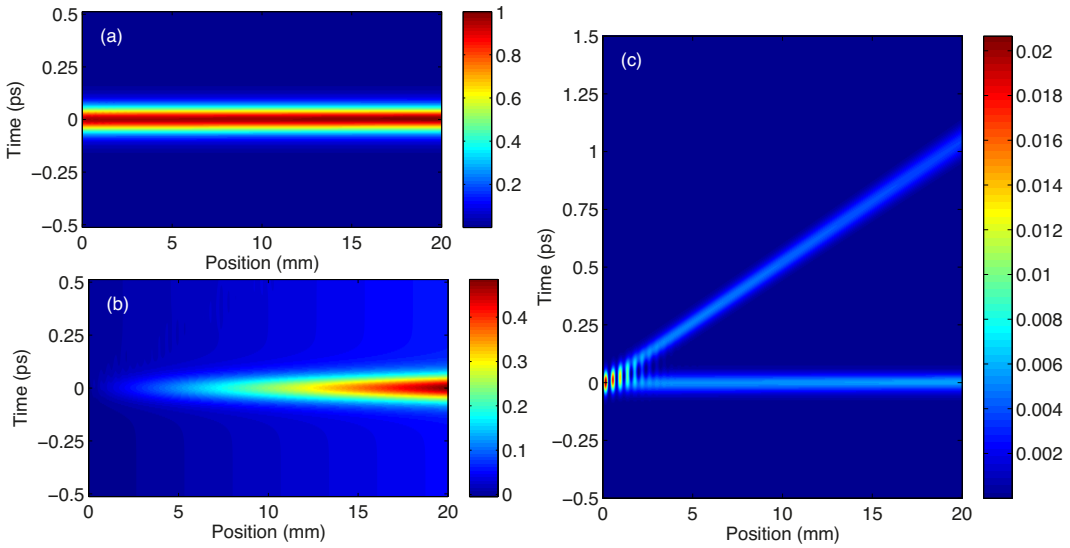

Fig. 1. Numerical simulation of a cascaded-$\chi^{(2)}$ interaction in a 20-mm-long LBO crystal, based on Eqs. (2). The simulation neglects transverse beam effects and diffraction for simplicity (plane-wave assumption). The parameters correspond closely to those we obtain in the experiments described in section 5. We assume a sech^2 input FH pulse of duration 100 fs (FWHM), and a phase mismatch of $\Delta k_0 = 15.5\ \mathrm{mm}^{-1}$. (a) Intensity of the FH, which remains largely unchanged. (b) Phase accumulated by the FH. From our choice of envelope definitions, with linear-optical propagation of form $\exp(-ikz)$, the positive nonlinear phase changes correspond to negative effective n_2^{NL}. (c) Intensity of the SH, showing the two pulse components described in the text. The pulse near time $t = 0$ ps leads to the SPM shown in (b), and interference between the two components can be seen near the input of the crystal. The second pulse clearly spreads in time: this occurs for two reasons: first, the GDD coefficient at the SH carrier frequency $\omega_2 = 2\omega_1$ is significantly larger than that at ω_1; and second, this SH component experiences no soliton shaping mechanism.

3.2. Frequency-domain analysis

In this subsection, we perform a perturbative frequency-domain analysis, assuming small nonlinear changes to the FH [47, 55]. A convenient form which is often practically relevant results when using Eq. (4b). If we first assume that the FH propagates linearly by setting the right hand side of Eq. (2a) to zero, it can be integrated over z in the optical-frequency and transverse-spatial frequency domains (frequency shift variable Ω and spatial frequency variables $\mathbf{k}_\perp = [k_x, k_y]$, respectively). The resulting FH envelope $A_1(z, \mathbf{k}_\perp, \Omega)$ can be substituted into Eq. (2b) in order to find, approximately, the behavior of the SH.

Since the resulting nonlinear term on the right hand side of Eq. (2b) is proportional to A_1^2, when expressed in the frequency domains it corresponds to a convolution integral over the FH spectrum. This convolution can be simplified if the phase mismatch depends only on the driven SH frequency and not on the intermediate frequency variable in the convolution [55]. This condition can be obtained by neglecting the contributions from diffraction and dispersion to Δk (i.e. by making a first-order expansion of Δk in its spatial and optical frequency variables). Under these approximations, we can define an accumulated phase mismatch for each spatial- and temporal-frequency according to

$$\Phi(z, k_x, \Omega) = [\Delta k_0 + (\delta_2 - \delta_1)\Omega + (\rho_2 - \rho_1)k_x]\, z. \tag{5}$$

#205464 - $15.00 USD Received 27 Jan 2014; accepted 25 Feb 2014; published 6 Mar 2014

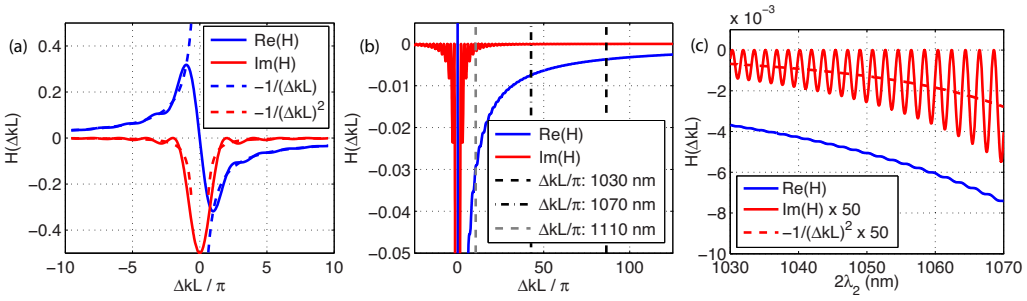

Fig. 2. Real and imaginary parts of the transfer function $H(\Phi)$ defined in Eq. (9b), as a function of phase $\Phi \sim \Delta kL$. (a) Profile of H, showing phase-matched and phase-mismatched regions, and the decay of the real and imaginary parts towards the region of large positive phase mismatch. (b) The same function as (a), but plotted over a different region and with a smaller y-scale; the vertical dashed and dash-dotted lines indicate the values of $\Delta kL/\pi$ for SHG of three different wavelengths in LBO (cut at zero degrees, with 1064-nm phase-matching at 149 °C); in our experiments we operate near 1050 nm, so in the region between the vertical black lines. (c) The transfer function zoomed into this region, and plotted as a function of wavelength rather than phase. To show its oscillatory character, the imaginary (loss-related) part has been multiplied by 50. The real part also oscillates, but with small relative amplitude in this region. Note, also, that in the nonlinear response of the FH [Eq. (8)], H takes argument $\Phi(k_x,\Omega)$, where this frequency-dependent accumulated phase mismatch is given by Eq. (5). As such, the complex form of H depicted in these figures can be applied both in the spatial and temporal domains.

where this form is similar to Eq. (4b) but including PVW in one transverse direction. For notational simplicity, we neglect the other transverse coordinate y. Integrating Eq. (2b) and applying Eq. (5), we find that

$$\tilde{A}_2(z=L,k_x,\Omega) = -i\kappa_2 L e^{-i(\rho_2 k_x+\delta_2\Omega)L}\frac{\exp\left[i\Phi(L,k_x,\Omega)\right]-1}{i\Phi(L,k_x,\Omega)}\mathscr{F}_{x,t}\left[A_1^2(z=0,x,t)\right] \qquad (6)$$

where $\mathscr{F}_{i,j,\ldots}$ denotes the Fourier transform with respect to the subscripted variables, and tilde denotes a variable expressed in the corresponding frequency domain(s). For sufficiently large Δk_0, the denominator can be approximated as $\Phi(L,0,0)$ (i.e. evaluated at zero optical and spatial frequency shifts) with only a small error in amplitude of $\tilde{A}_2$. We can then return to the time-domain to arrive at a simple form for the SH:

$$A_2(L,x,t) = -\frac{\kappa_2}{\Delta k_0}\left[A_1^2(0,x+\rho_1 L,t+\delta_1 L)e^{i\Delta k_0 L} - A_1^2\left(0,x+\rho_2 L,t+\delta_2 L\right)\right]. \qquad (7)$$

This equation clearly shows the presence of two pulse components, one propagating with the FH and the other propagating linearly, as in Fig. 1. The former component accumulates phase shift $\exp(i\Delta k_0 z)$, which cancels with the $\exp(-i\Delta k_0 z)$ factor on the right hand side of Eq. (2a), which allows for SPM of the FH.

Next, to find the response of the FH, we make the same approximations and substitute Eq. (6) into Eq. (2a). After some algebra, we find the following:

$$A_1(L,x-\rho_1 L,t-\delta_1 L) = A_1(0,x,t) - iLA_1^*(0,x,t)\mathscr{F}_{x,t}^{-1}\left[\mathscr{F}_{x,t}\left[A_1^2\right]Q\right](0,x,t), \qquad (8)$$

#205464 - $15.00 USD Received 27 Jan 2014; accepted 25 Feb 2014; published 6 Mar 2014

where the transfer function $Q = Q(k_x, \Omega)$ appearing in this equation is given by

$$Q(k_x,\Omega) = -\kappa_1\kappa_2 L\left(\frac{e^{-i\Phi(L,k_x,\Omega)}-1}{i\Phi(L,k_x,\Omega)^2} + \frac{1}{\Phi(L,k_x,\Omega)}\right) \tag{9a}$$

$$\equiv \kappa_1\kappa_2 L H(\Phi(L,k_x,\Omega)) \tag{9b}$$

with Φ given by Eq. (5). Eq. (8) resembles a Raman-like response [56], as shown by other treatments of cascading interactions [38]. We note that an alternative approach to the above analysis would be to use frequency-domain envelopes B_j, defined to account for all linear propagation effects such that $\partial_z B_j = 0$ for linear-optical propagation [55]. Recently, this technique was extended to obtain a general formalism for pulse synthesis via frequency conversion, focusing on quasi-phase-matching (QPM) devices [57].

The utility of Eq. (8) is that it captures the effects of the multiple SH pulse components as well as resonant (phase-matched) effects. These can be seen by plotting $H(\Phi)$ defined in Eq. (9b), as shown in Fig. 2. For large Φ, the imaginary (lossy) part decays as $1/\Phi^2$ while the real (SPM) part only decays as $1/\Phi$, which indicates how large nonlinear phase shifts can be obtained without incurring large nonlinear losses; we revisit this trade-off in section 4. The oscillatory character of $H(\Phi)$ gives rise to multiple pulse components, associated with the two SH components given in Eq. (7); if the range of Φ spanned by the spatial (temporal) frequencies of $A_1^2(0,x,t)$ is large, e.g. 2π, then the multiple components are separated in space (time). Furthermore, if either of these ranges approaches $\Phi = 0$, then there can be efficient up-conversion as well as a non-uniform real part of the transfer function, giving rise to stronger nonlinear losses and to a non-instantaneous nonlinear response.

While Eq. (8) shows these important features, its applicability is limited because it assumes small nonlinear changes to the FH, and because it applies only for PVW- and GVM-dominated interactions. Furthermore, because Eq. (8) accounts for nearly-phase-matched spectral components as well as highly phase-mismatched ones, its form is less intuitive. In the next subsection, we perform an alternative, often more general analysis, which captures the relevant features in a more intuitive way.

3.3. Multiple-scale analysis

As mentioned above in section 2, the characteristic property of cascading interactions is a large phase mismatch Δk. This property enables a perturbative analysis of the interaction based on multiple-scale analysis, as introduced in [58]. In [58], the combined effects of cascading and diffraction were considered to first order in this perturbation, yielding effective lensing effects. A similar procedure can be performed with operators $\hat{D}_j$ introduced in Eqs. (2) for linear-optical propagation, capturing both spatial and temporal effects. In this more general situation, the approximation is based on the length scale $L_{coh} = \pi/|\Delta k|$ being sufficiently short compared with the other characteristic lengths of the interaction. These characteristic lengths include group velocity walk-off, Poynting vector walk-off, pulse and beam spreading due to dispersion and diffraction, respectively, and the nonlinear length characterizing the rate of coupling between the fields [45, 59].

To include losses and the non-instantaneous character of the nonlinearity, we go to second order in the perturbation and account for boundary conditions of the crystal and laser cavity. The fields are split up into components at orders ε^n of the perturbation parameter $\varepsilon \propto L_{\mathrm{coh}}$; we omit the mathematical details of the derivation. The $\mathrm{O}(\varepsilon^0)$ (leading-order) components, denoted $A_j^{(0)}$, vary slowly, i.e. on spatial scales $\gg L_{coh}$. For SHG-type cascading interactions with zero input SH, the leading-order component of the SH is zero [58]. Experimentally, this corresponds to the assumption that any SH leaving the crystal is not recirculated by the cavity. Under this

#205464 - $15.00 USD Received 27 Jan 2014; accepted 25 Feb 2014; published 6 Mar 2014

assumption, the generated SH is given, to first order ($\propto |1/\Delta k_0|$), by

$$A_2^{(1)}(z,x,t) = -\frac{\kappa_2}{\Delta k_0}\left[(A_1^{(0)}(z,x,t))^2 e^{i\Delta k_0 z} - a_2^{(1)}(z,x,t)\right] \tag{10}$$

where $a_2^{(1)}$ is a boundary condition term. This term satisfies $a_2^{(1)}(0,x,t) = (A_1^{(0)}(0,x,t))^2$, such that the term in square brackets is initially zero. Thereafter, $a_2^{(1)}$ propagates linearly, according to $(\partial_z + \hat{D}_2)a_2^{(1)} = 0$. Eq. (10) is in fact a more general form of Eq. (7).

The leading-order component of the FH evolves, to second order in the approximation, according to

$$\left(\partial_z + \hat{D}_1\right)A_1^{(0)} = i\frac{\kappa_1\kappa_2}{\Delta k_0}|A_1^{(0)}|^2 A_1^{(0)} + \frac{\kappa_1\kappa_2}{\Delta k_0^2}\left[2|A_1^{(0)}|^2\hat{D}_1\left(A_1^{(0)}\right) - A_1^{(0)*}\hat{D}_2\left((A_1^{(0)})^2\right)\right] \tag{11}$$

The energy in this $A_1^{(0)}$ component is reduced compared to the incident energy due to the nonlinear losses associated with Eq. (10). We have checked the behavior of Eq. (11) numerically based on Eqs. (2) in a configuration similar to our experiments, and found that it quantitatively captures the most important dynamical features. For this configuration, the $\hat{D}_2$-dependent term in Eq. (11) is the dominant second-order [i.e. $O(1/\Delta k_0^2)$] dynamical process. If we neglect dispersion and diffraction, then $\hat{D}_2 = \rho_2\partial_x + \delta_2\partial_t$, and hence the $\hat{D}_2$-related term in Eq. (11) involves temporal and spatial derivatives of A_1^2, which correspond to non-instantaneous/non-local terms in the nonlinear response.

In the case of low-loss cavities, the net SPM or B-integral can be calculated in the usual way, using Eq. (1) to augment the description of nonlinear phase shifts based on true $\chi^{(3)}$ effects occurring in the gain and SHG crystals; the value of n_2^{casc} can be derived from the $O(|1/\Delta k_0|)$ term in Eq. (11). The influence of GVM effects, caused by the $\hat{D}_2$ term in Eq. (11), can be minimized by keeping $L_{GVM} \gg L_{coh}$. We revisit this point in section 4. In addition to SPM, there is a TPA-like nonlinear loss due to the generated SH. Summing the energies of the two SH pulse components in Eq. (10) and taking the ratio of this sum to the energy in the FH, this loss can be approximated as

$$a_{NL} = \frac{4}{3}\frac{\omega_1^2 d_{\text{eff}}^2}{n_1^2 n_2 \varepsilon_0 c^3}\frac{I_{1,pk}}{\Delta k_0^2}, \tag{12}$$

where $I_{1,pk}$ is the peak intensity of the FH in space and time, and where this equation assumes a Gaussian spatial profile and a sech^2 temporal profile. The same nonlinear loss can be obtained from Eq. (7) or from Eq. (8). This loss should usually be minimized so as to avoid multi-pulsing. It is important to note, however, that such a variable nonlinear loss can actually be highly advantageous for GHz lasers, since it could allow for optimal suppression of Q-switching instabilities [48, 60, 61].

As well as the leading-order behavior captured by Eq. (11), the secondary pulse in Eq. (10) introduces an additional FH pulse component, since, at $z = L$,

$$A_1 \approx A_1^{(0)} + \frac{\kappa_1\kappa_2}{\Delta k_0^2}e^{-i\Delta k_0 L}A_1^{(0)*}a_2^{(1)}. \tag{13}$$

Because $a_2^{(1)}$ and $A_1^{(0)}$ travel at different velocities, this extra term is an etalon-like distortion, in that it corresponds to an additional FH pulse component which is temporally separated from the main one. The same effect is described by the transfer function H in Eq. (9b). However, with the approach taken in this subsection, the equations take on a more intuitive form, and we do not have to assume small phase shifts or small nonlinear losses.

#205464 - $15.00 USD Received 27 Jan 2014; accepted 25 Feb 2014; published 6 Mar 2014

Etalon effects can make it more difficult to achieve self-starting modelocking [62]. However, the impact of the additional pulse component on modelocking emerges only after performing an overlap integral of the output FH with the appropriate cavity mode profile. Since a_2 is initially overlapped with $A_1^{(0)}$ in space and time and subsequently evolves according to $\hat{D}_2$, it can separate from the FH mode laterally in space as well as time. The separation in space reduces the overlap integral, while the separation in time both minimizes the overlap of the two pulse components.

4. Design considerations

In this section, we use the results of section 3 to find practical design constraints for SESAM-based modelocking, in particular for the laser which we will present in section 5 (Fig. 4). There are several factors to consider. These include basic considerations such as the choice of gain crystal, pumping conditions, and intensities, as well as the choice of SHG crystal and the cavity design. The total cavity GDD should not be too large, since for a given pulse duration the required total SPM scales with GDD, according to the standard soliton formula [56].

For the cascading interaction itself, there is, at a given pulse intensity, a trade-off between crystal length and phase mismatch in terms of:

1. Accumulating sufficient negative SPM via cascading, obtained via small Δk_0 and/or large L, and characterized by Eq. (1)];
2. Minimizing nonlinear losses due to SHG: these are characterized, per pass through the crystal, by Eq. (12), and are *independent* of length L.
3. Adding unwanted GDD by using a longer crystal. This GDD scales with L, as does the SPM.

In addition to Eqs. (1) and (12), a useful relation for the nonlinear losses in terms of the cascading-induced SPM which emphasizes the above trade-off is given by

$$a_{NL} = \frac{4}{3\Delta k_0 L}\phi_{NL}, \tag{14}$$

where ϕ_{NL} is the accumulated nonlinear phase from the cascading process, given by $\phi_{NL} = \int_0^L (2\pi/\lambda_1) n_2^{\mathrm{casc}} I_1(z) dz$ for FH intensity $I_1(z)$ and effective nonlinear refractive index n_2^{casc} given by Eq. (1).

Regarding point 3 above: bulk temporal solitons are supported via the positive GDD and negative SPM present in the SHG crystal, so that in the absence of any other cavity dispersion or nonlinearity, increasing the crystal length at a given pulse intensity does not alter the soliton formation, at least to the extent that lensing and diffraction effects remain negligible. However, when there is GDD and SPM from other intracavity elements (in particular, the gain crystal), the SHG crystal must 'work harder' to enable soliton formation than it would otherwise, for example by being operated closer to phase-matching (and hence incurring larger nonlinear losses). Regarding point 2 above, the tolerable nonlinear losses are coupled to the SESAM parameters, in particular its modulation depth, saturation fluence, and roll-over characteristics of its nonlinear reflectivity [8, 61]. In analogy to conventional SESAM modelocking, multi-pulsing can occur when operating in the roll-over regime.

As well as the above issues, there are a number of other constraints. For example, avoiding GVM-related effects corresponding to the $O(1/\Delta k_0^2)$ terms in Eq. (11) requires that the GVM length $L_{GVM} = \tau_{\mathrm{FWHM}}/|\delta_2 - \delta_1| > L_{coh} = \pi/|\Delta k_0|$ for full-width at half-maximum (FWHM) pulse duration τ_{FWHM}, i.e. that pulse walk-off occurs slowly compared to the rapid oscillation

#205464 - $15.00 USD Received 27 Jan 2014; accepted 25 Feb 2014; published 6 Mar 2014

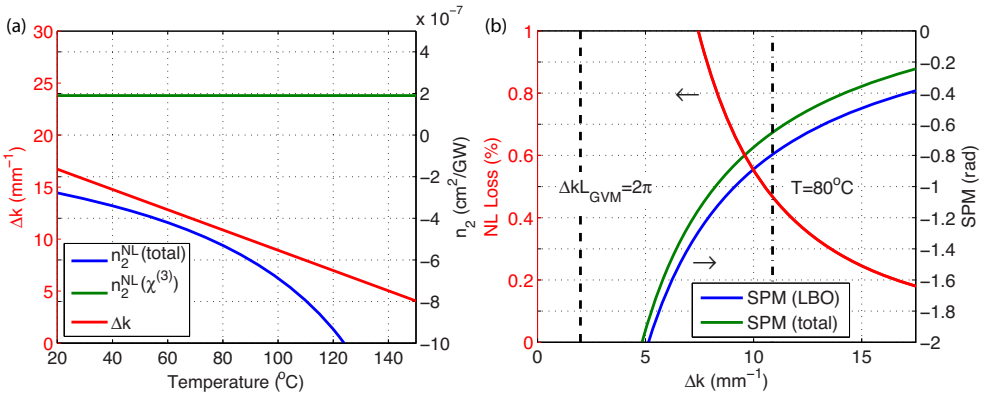

Fig. 3. (a) Phase mismatch Δk and nonlinear refractive index n_2^{NL} as a function of LBO crystal temperature for a center wavelength of 1050 nm, assuming an angle of $\phi = 2^\circ$. Both the assumed intrinsic $\chi^{(3)}$-related n_2^{NL}, and the total effective n_2^{NL} from both cascading and $\chi^{(3)}$, are shown. (b) Nonlinear losses and SPM as a function of phase mismatch Δk, for a particular laser configuration, with parameters chosen based on our experiments (see section 5). Estimates of the SPM from the LBO crystal as well the total SPM are shown; this total SPM includes contributions from the LBO crystal, the Yb:CALGO gain crystal, and a small contribution from the YAG Brewster plate. The dashed vertical line shows the values of Δk at which $\Delta k L_{GVM} = 2\pi$ (where we would expect GVM-related effects to be significant). The dot-dashed vertical line indicates the Δk value corresponding to a temperature of 80 °C, which is relevant to our experiments. Note that we operate very far from the $\Delta k L_{GVM} = 2\pi$ condition. (a) shows that the intrinsic $\chi^{(3)}$ nonlinearity of LBO cannot be ignored for our case, and (b) shows the trade-off between nonlinear losses and SPM, and that the SPM from the gain crystal cannot be ignored either.

of $\exp(\pm\Delta k_0 z)$ in the parametric driving terms. An analogous condition can apply to PVW, i.e. $L_{wo} = w/|\rho_2 - \rho_1| > L_{coh}$ for $1/e^2$ beam radius w.

However, based on the modal overlap discussion in the preceding section, some PVW is advantageous in order to suppress or reduce the severity of nonlinear etalon-type effects. GVM is also advantageous in this context, since it either allows the SESAM to recover after the main pulse (if the SH travels slower than the FH within the nonlinear crystal) or causes the weak secondary pulse described by Eq. (13) to see an unsaturated SESAM (if the SH travels faster than the FH). Based on these considerations, it can actually be advantageous to operate in a regime with large group-velocity- and Poynting-vector-walkoff, in contrast to conventional SHG interactions. As such, configurations satisfying the inequalities

$$L > L_{wo} > L_{coh} \tag{15a}$$

$$L > L_{GVM} > L_{coh} \tag{15b}$$

are favorable. In certain configurations, diffraction effects could be important, as well as the crystal damage threshold. To elucidate several of the design considerations discussed above, we show characteristic features of the interaction as a function of Δk_0, varied via crystal temperature, in Fig. 3.

5. Experimental setup and results

Based on the results of the previous sections, we designed and constructed a modelocked laser exploiting cascading in order to achieve self-starting SESAM modelocking in the positive dis-

#205464 - $15.00 USD Received 27 Jan 2014; accepted 25 Feb 2014; published 6 Mar 2014

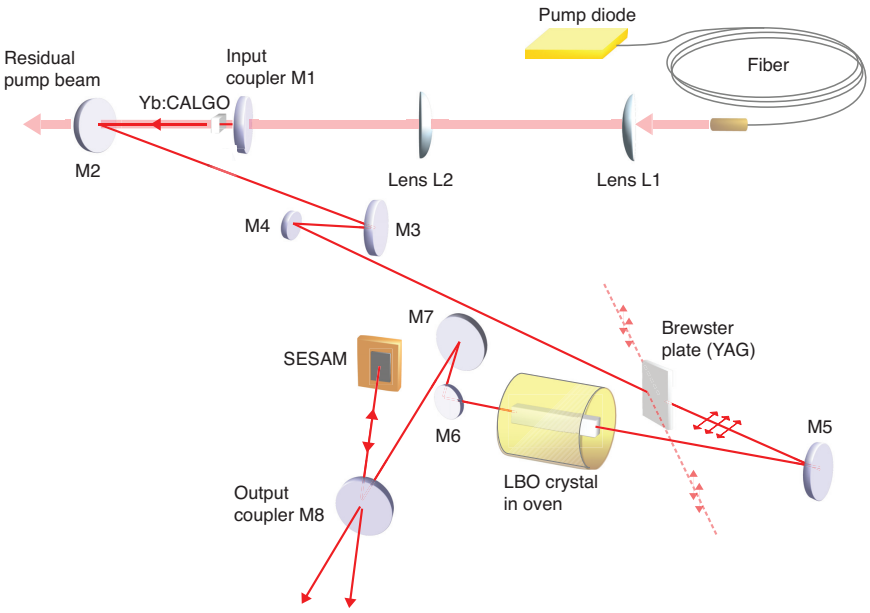

Fig. 4. Schematic of the laser. The pump beam goes through the laser cavity end mirror M1 and is coupled out through mirror M2. Given the chosen beam size in the gain crystal, mirrors M2-M5 yield a small spot size in the LBO crystal, while mirrors M6-M8 ensure a larger spot size on the SESAM, necessary not to over-saturate it. The resulting spot sizes are given in the text. The cavity was designed to obtain these beam sizes without being too sensitive to length offsets or close to the edge of stability. The mirror curvatures are as follows: $R_{M2} = 150$ mm; $R_{M3} = 400$ mm; $R_{M5} = 300$ mm; $R_{M7} = 200$ mm; remaining mirrors: flat. All laser cavity mirrors M1-M7 are standard highly reflective Bragg mirrors without any GDD within the pulse spectrum.

persion / negative SPM regime, without the need for any dispersion compensating elements. We chose the relatively new material Yb:CALGO [63] in order to support broad bandwidths, and more generally because of the material's great promise in terms of short-pulse power scaling in the near future [63–69]. We use LBO to obtain negative SPM as it is well-suited to SHG-type interactions around 1 μm, and high-quality crystals are readily available.

5.1. Experimental setup

The linear-cavity laser is depicted in Fig. 4. The $1/e^2$ beam radii in the Yb:CALGO and LBO crystals were, respectively, $\approx$156 μm and $\approx$99 μm. The 20-mm-long AR-coated LBO crystal was cut at $\theta = 90°$ and $\phi = 0°$, corresponding to phase-matching for 1064-nm SHG at 149 °C (specified by the manufacturer), and was operated at various temperatures $\leq$ 100 °C. The beam radius on the SESAM was $\approx$321 μm with a slight ellipticity, and the SESAM used was measured to have a saturation fluence of 5.8 μJ/cm^2 and a modulation depth of 2.8%. The transmission of the output coupler, which the laser beam passes twice, was 1.6%, and the remaining mirrors are highly reflective for the laser wavelength. No dispersion-compensating elements were used. A 1.5-mm-thick YAG Brewster plate was used for astigmatism compensation. The laser light is horizontally polarized.

To pump the laser, we used a multimode diode with a center wavelength of $\approx$ 980 nm and

#205464 - $15.00 USD Received 27 Jan 2014; accepted 25 Feb 2014; published 6 Mar 2014

a bandwidth of ≈ 5 nm; the center wavelength varied over a range of ~ 5 nm for the range of currents used in the experiment (slope 0.8 nm/A), with better spectral overlap with the 980-nm absorption peak of Yb:CALGO occurring at the higher currents. The output pump power used was 0 - 13 W, out of a maximum possible 25 W. The multimode pump beam was focused to approximately the same size as the laser beam in the gain crystal, situated immediately after the laser cavity end mirror M1 shown in Fig. 4. The Yb:CALGO crystal had a nominal doping concentration of 5% and was 3 mm long.

5.2. Experimental results

The best performance obtained with this proof-of-principle laser was 1.1 W average output power (counting both output beams from the output-coupler; ≈ 34.5 W intracavity) at 113 MHz repetition rate (304 nJ intracavity pulse energy), generating 114-fs sech^2 pulses, as indicated by the autocorrelation in Fig. 5(a). Fig. 5(b) shows the output spectrum (FWHM bandwidth 10.5 nm, center wavelength of 1050 nm). The time-bandwidth product (TBP) was 0.329, indicating nearly transform-limited sech^2 pulses, i.e. an ideal soliton pulse as expected from soliton modelocking. Figures 5(c) and 5(d) show the radio frequency (RF) spectrum of the pulse train, measured with a high-speed photodiode, the signal of which was amplified with a 1.3 GHz-bandwidth amplifier prior to the RF spectrum analyzer. We confirmed single-pulse operation with a sampling oscilloscope in addition to the Femtochome autocorrelator. The laser was always self-starting.

The above performance was obtained when operating the LBO crystal at 80 °C and orienting it at an internal angle (inside the crystal) of $\phi \sim 2^\circ$ in the horizontal plane (yielding a larger positive Δk compared with $\phi = 0^\circ$). This angle also introduces a Poynting vector walk-off of the FH (but not the SH, which is polarized vertically). Operation with such non-negligible angles was important in obtaining reliable self-starting operation in the single-pulsing regime. Based on Eq. (10), the PVW yields a partial suppression of the oscillations in Fig. 2. Due to the long crystal length, much smaller angles of the LBO crystal would still be sufficient to suppress linear back-reflections from imperfect anti-reflection coatings. And, by adjusting the temperature, the same phase mismatch could be obtained at these smaller angles. Therefore, the improved performance when operating at crystal angles large enough to introduce non-negligible PVW suggests that the oscillations in Fig. 2 indeed hinder (but do not necessarily preclude) self-starting.

For a given set of nonlinear crystals inside the laser cavity, the negative SPM from the cascaded $\chi^{(2)}$ crystal must sufficiently exceed the positive SPM contributions from all the crystals, and be balanced by the net positive GDD. Furthermore, excessive nonlinear losses via SHG will favor double-pulsed operation. Obtaining a large SPM and minimal losses requires operating at a sufficient phase mismatch $|\Delta k|$, based on Fig. 3. Indeed, the pulse durations we could achieve without dispersion compensation were limited by nonlinear losses: the duration decreases as the power increases, until the laser jumps to a double- or multi-pulsed configuration (corresponding to lower losses). This multi-pulsing issue is not a fundamental limit, as it can be avoided by a combination of cavity, LBO, laser crystal, and SESAM design. Since we already achieved 114 fs in this first demonstration, we can anticipate $\ll$100 fs pulses for an optimized laser configuration in the near future.

To explore the modelocking regime, we show several scans of laser performance versus different parameters in Fig. 6. In Fig. 6(a), the pulse duration is shown as a function of output power for several different temperatures of the cascading crystal. As expected for solitons, the pulse duration decreases with laser power. Lower temperatures correspond to larger phase mismatches and hence reduced effective n_2^{NL}, which in turn leads to longer pulses at a given power. However, while the pulses are shorter at higher temperatures, the maximum power while

#205464 - $15.00 USD Received 27 Jan 2014; accepted 25 Feb 2014; published 6 Mar 2014

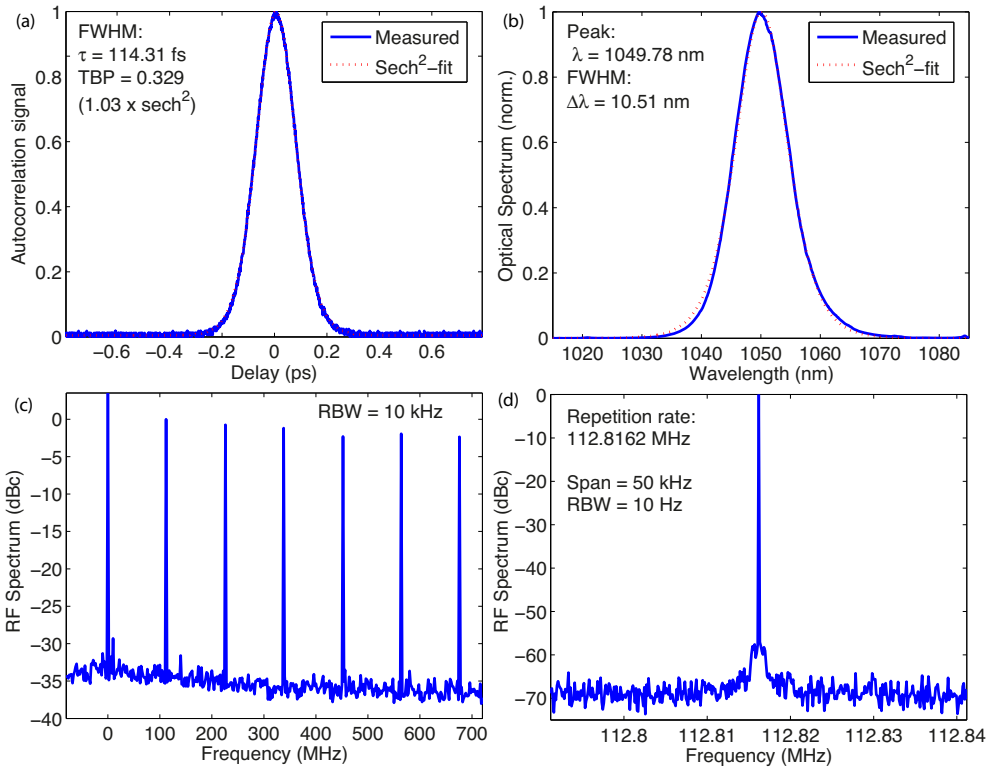

Fig. 5. Characterization of the SESAM modelocked Yb:CALGO laser performance, operating in the soliton modelocking regime using positive intracavity GDD and an effective "negative SPM" via phase-mismatched SHG in LBO. The LBO crystal temperature was set to 80 °C. (a) SHG autocorrelation of the 1050-nm laser output. (b) Optical spectrum, measured with an optical spectrum analyzer. (c) Radio frequency (RF) spectrum, showing several harmonics within the bandwidth of the RF amplifier following a high-speed photodiode. RBW: resolution bandwidth. (d) RF spectrum, zoomed into the first harmonic.

maintaining single-pulse operation decreases with temperature due to the higher SHG losses: for even higher temperatures than those shown, the single-pulse-modelocking range vanishes. Note that, in order to avoid the risk of damaging the input-coupling mirror M1, we did not increase the pump power further than the range shown in Fig. 6.

In Fig. 6(b), we show the SHG power generated, found by measuring the green light leaving the cavity in one direction (behind mirror M5), accounting for the IR and green transmission of the mirror M5, and multiplying by two to account for the green generated in the other direction, going towards mirror M6, which we assume has equal power to the measured component. There is a clear trend for increasing green power when operating closer to phase-matching. In Fig. 6(c), we show similar features but parameterized in terms of the intracavity peak power and nonlinear losses. These losses are nearly linear in peak power, as expected from Eq. (12). Moreover, Fig. 6(d) shows the losses versus peak power divided by Δk_0^2: as also expected from Eq. (12), the curves for the different temperatures coincide, which supports the theory and further confirms that we are currently limited by these losses.

#205464 - $15.00 USD Received 27 Jan 2014; accepted 25 Feb 2014; published 6 Mar 2014

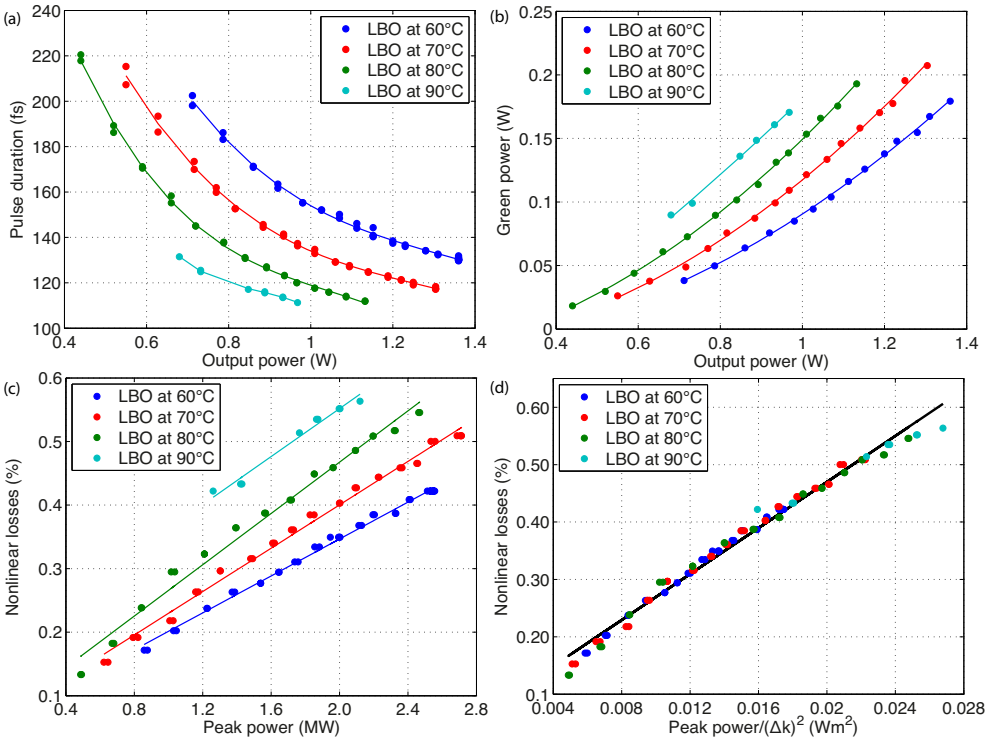

Fig. 6. Scans of laser modelocked operation as a function of various parameters, for several different temperatures of the LBO crystal. (a) Pulse duration versus laser average output power. (b) Generated SHG as a function of output power. (c) Nonlinear losses associated with the SHG process shown in (b), plotted versus intracavity peak power, showing a near-linear dependence for each temperature. The pulse durations for higher temperatures (e.g. 90 °C) are limited by the transition to multi-pulsed regime at higher powers. For lower temperatures (e.g. 60 °C), we limited the pump power used in order to minimize the chance of damaging the input coupling mirror M1. (d) Nonlinear losses shown in (c), but with a rescaled x-axis to confirm the theoretically-predicted $1/\Delta k^2$-dependence of these losses.

6. Conclusions

Our results represent the first SESAM modelocked laser using cascaded quadratic nonlinearities to achieve soliton modelocking in the 100-fs regime, to the best of our knowledge. Furthermore, this performance was achieved with the relatively new and very promising Yb:CALGO gain crystal [63]. This gain crystal will support scaling of both the power and pulse duration in the near future [64]. The laser was self-starting and did not rely on Kerr-lens modelocking, which is another important practical advantage.

In addition to modern SESAM and laser-crystal technology, our results were made possible by a detailed analysis of soliton modelocking using cascaded $\chi^{(2)}$ effects. The theoretical and design analysis presented in sections 3 and 4 both summarize existing work relevant to modelocking, and extend the theory in an accurate but intuitive way. Our analysis of the cascading dynamics clearly indicated the advantages of laser designs using the strong GVM regime for modelocking. This regime allowed us to overcome the limitations of previous SESAM modelocking experiments utilizing cascading, thereby reaching the femtosecond regime. To obtain reliable self-starting behavior, it was also important to operate the LBO crystal at a moder-

#205464 - $15.00 USD Received 27 Jan 2014; accepted 25 Feb 2014; published 6 Mar 2014

ate angle of incidence, sufficient to introduce non-negligible Poynting vector walk-off between the two generated SH pulse components. Spatial and temporal separation of these components minimizes the influence of the secondary, dispersive pulse on the fundamental cavity mode of the FH. The operating regime thus involved strong GVM and significant PVW, and hence is drastically different than conventional phase-matched interactions.

Optimization of both the SPM and the nonlinear losses associated with the modelocking process based on the analysis presented enabled nonlinear losses at the $\lesssim 0.5\%$ level, consistent with our theoretical predictions. These losses were small enough to allow modelocking with a $<3\%$ modulation depth SESAM. In order to achieve low-noise operation, it is favorable to use high-Q optical cavities [70]. Given such a high-Q cavity, using a low SESAM modulation depth is important in order to avoid Q-switching instabilities [60].

Our experimental and theoretical results will be crucial in deploying the cascading technique in additional laser architectures and in practical modelocked lasers in general. For example, future demonstration of the technique in a disk-laser configuration is especially promising, since this would enable power scaling while simultaneously minimizing the unwanted SPM and GDD arising from the gain medium. Such a configuration would allow for shorter nonlinear crystals, lower SPM, and lower nonlinear losses. The dispersion and nonlinearity in the cavity arises from inherent material properties, and should therefore be very reliable and repeatable without placing strict demands on dielectric mirror growth. Operation with periodically poled lithium niobate (PPLN) or other QPM materials would give access to orders of magnitude larger nonlinearities, especially relevant to the lower pulse energies present in GHz lasers, where the lower peak powers and restricted cavity design space make it much more challenging to achieve large nonlinear phase shifts and dispersion compensation.

In summary, the technique we have presented holds great promise in a wide variety of state-of-the-art solid-state SESAM-modelocked laser systems, and may overcome several of the important limiting factors associated with conventional soliton modelocking in these lasers.

Acknowledgments

This research was supported by a Marie Curie International Incoming Fellowship within the 7th European Community Framework Programme, by ETH Research Grant ETH-26 12-1, and by the ERC advanced grant ERC-2012-ADG_20120216 within the seventh framework programme of the European Union.